

End-to-end reconstruction of OCT optical properties and speckle-reduced structural intensity via physics-based learning

Jinglun Yu^a, Yaning Wang^a, Wenhan Guo^{a,b}, Yuan Gao^a, Yu Sun^{a,b}, and Jin U. Kang^a

^aDepartment of Electrical and Computer Engineering, Johns Hopkins University, Baltimore, USA

^bData Science and AI Institute, Johns Hopkins University, Baltimore, USA

ABSTRACT

Inverse scattering in optical coherence tomography (OCT) seeks to recover both structural images and intrinsic tissue optical properties, including refractive index, scattering coefficient, and anisotropy. This inverse problem is challenging due to attenuation, speckle noise, and strong coupling among parameters. We propose a regularized end-to-end deep learning framework that jointly reconstructs optical parameter maps and speckle-reduced OCT structural intensity for layer visualization. Trained with Monte Carlo-simulated ground truth, our network incorporates a physics-based OCT forward model that generates predicted signals from the estimated parameters, providing physics-consistent supervision for parameter recovery and artifact suppression. Experiments on the synthetic corneal OCT dataset demonstrate robust optical map recovery under noise, improved resolution, and enhanced structural fidelity. This approach enables quantitative multi-parameter tissue characterization and highlights the benefit of combining physics-informed modeling with deep learning for computational OCT.

Keywords: Optical coherence tomography (OCT), tissue characterization, speckle reduction, inverse problem, physics-informed deep learning, diffusion model

1. INTRODUCTION

Optical coherence tomography (OCT) acquires high-resolution cross-sectional images by measuring backscattered interferometric signals.^{1,2} It has become a widely used modality for microstructure assessment, disease diagnosis, and biomedical imaging.^{3–6} However, the contrast in OCT intensity arises from only a narrow range of variations in intrinsic refractive index (typically 1.3–1.5),⁷ and backscattered signals are significantly affected by attenuation and speckle noise during light propagation. As a result, using only the OCT intensity signal often struggles to recover detailed structural information, especially in complex tissues containing fuzzy boundaries and heterogeneous compositions.⁸

To obtain the more accurate tissue anatomy, there has been increasing interest in recovering intrinsic optical properties from OCT intensity by solving the associated inverse problem. These parameters enable a more meaningful physical characterization of the tissue including refractive index, scattering coefficient, and anisotropy.⁹ However, the inverse problem is severely ill-posed: multiple unknown parameters are strongly coupled, OCT signal amplitude decays with depth, noise propagates through the OCT signal formation process, and reconstructions require suitable priors for stability.¹⁰ Traditional approaches typically rely on Beer–Lambert attenuation modeling, exponential fitting, or iterative regularization.^{11–13} While effective under restricted assumptions, these methods are noise-sensitive, often require segmentation or depth discretization, and tend to oversmooth or degrade spatial continuity.¹⁴

Deep learning has recently been explored for OCT signal reconstruction and optical parameter characterization.¹⁵ However, supervised models require extensive datasets with ground-truth parameters, which are difficult to obtain experimentally, limiting generalization to diverse tissues or imaging conditions.¹⁶

To address these challenges and enable joint recovery of multi-parameter tissue maps, we propose a regularized end-to-end deep learning framework with a multi-channel encoder-decoder backbone, in which a physics-based OCT forward model is embedded as a differentiable constraint. From predicted refractive index, scattering coefficient, and anisotropy, the network computes theoretical OCT signals and enforces consistency with measured intensities, enabling simultaneous learning of tissue scattering behavior and speckle-reduced structural intensity maps. In a single pass, the framework provides noise-robust optical maps together with improved structural visibility for label-free layer visualization. Validation on Monte Carlo-simulated corneal datasets ($N > 500$) demonstrates robust recovery of structural information from OCT intensity under noise.

2. METHODS

We propose an end-to-end OCT inverse reconstruction framework that performs single-pass inference to simultaneously recover intrinsic tissue optical properties and speckle-reduced OCT structural intensity, as shown in figure 1. The framework consists of two major components: (1) a U-Net-based multi-channel mapping network for optical properties reconstruction, and (2) a differentiable physics-based OCT forward model used as a consistency constraint during training.

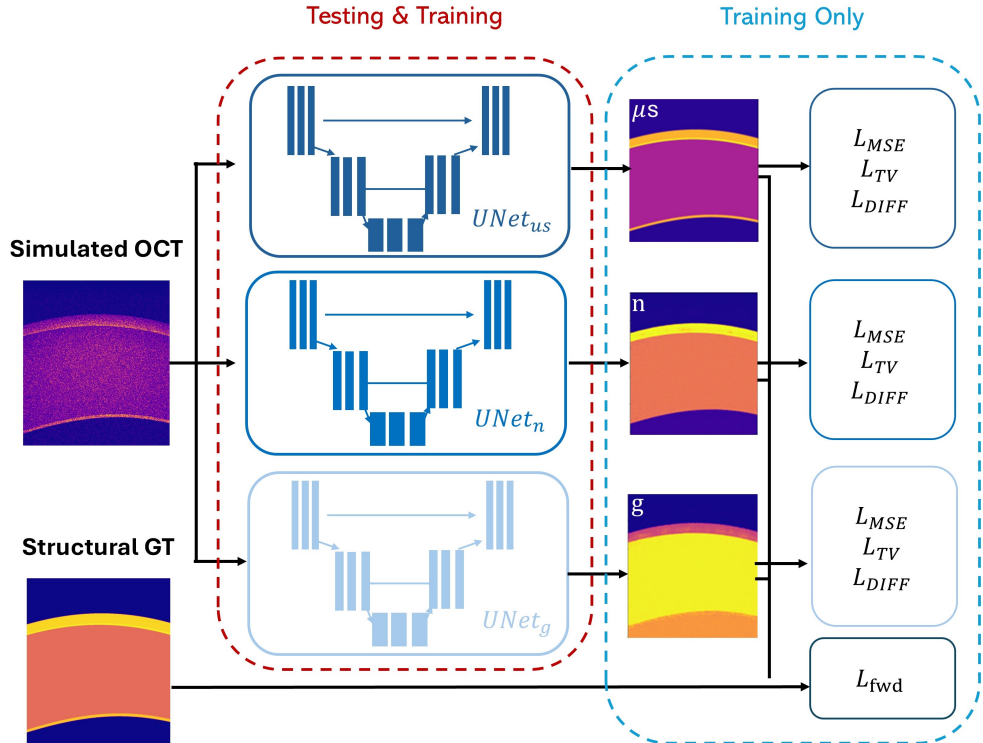


Figure 1. End-to-end physics-regularized framework for OCT inverse scattering. Red box: U-Net predictors used for both training and testing; blue box: loss modules applied only during training.

2.1 Network Architecture

The network input is the raw OCT B-mode image \mathbf{I}_{raw} (Monte Carlo simulated 1024×1024). The dataset contains 500 corneal images synthesized based on prior geometric models of human corneal anatomy.¹⁷ The network outputs three optical property maps—refractive index $n(x, y)$, scattering coefficient $\mu_s(x, y)$, and anisotropy $g(x, y)$ —together with the speckle-reduced predicted OCT structural intensity $\hat{\mathbf{I}}(x, y)$.

The backbone adopts a U-Net-style encoder-decoder structure with four downsampling-upsampling stages and skip connections that preserve high-frequency spatial detailS. Convolution kernels of size 3×3 and Batch-Norm layers are used in each stage; these hyperparameters were empirically tuned to achieve a balance between receptive-field size, computational cost, and training stability without oversmoothing. Each optical property is predicted through an independent U-Net branch rather than a shared backbone, ensuring that the optimization trajectories remain fully decoupled across n , μ_s , and g . Although several loss terms (e.g., forward consistency) are applied simultaneously to all branches, network weights and gradients are not shared, preventing implicit interference between branch-specific representations.

2.2 Physics-based Forward Model Constraint

To establish a physical relationship between the estimated optical properties and the measured OCT intensity, we embed a differentiable OCT forward model into the training pipeline. The forward model is inspired by the Extended Huygens-Fresnel (EHF) theory for multiply scattered OCT signals, in which the mean squared OCT amplitude $A(z)$ (equivalent to the OCT intensity \hat{I}_{OCT}) along depth z is composed of three contributions: (i) single scattering, (ii) multiple forward scattering, and (iii) the coherent cross-term between them.¹⁸

Under the paraxial approximation and a highly forward-scattering regime ($g > 0.7$), the EHF formulation defines the local beam waist in the absence of forward scattering, denoted as $w_H(z)$, and its broadened counterpart $w_S(z)$ when multiple forward scattering is present. These quantities depend on system beam parameters, including the beam waist radius w_0 , the Rayleigh length z_R , and the focal depth z_f , as well as on the anisotropy-dependent scattering angle $\theta_{\text{RMS}} \approx \sqrt{2(1-g)}$, which jointly result in depth-dependent beam propagation, reduced lateral resolution, and speckle blurring.

A differentiable approximation of the EHF forward model is implemented as

$$\langle A^2(z) \rangle \propto \frac{1}{w_H^2(z)} \left\{ \exp(-2\mu_s z) + 4 \exp(-\mu_s z) \frac{[1 - \exp(-\mu_s z)]}{1 + \frac{w_S^2(z)}{w_H^2(z)}} + \frac{[1 - \exp(-\mu_s z)]^2 w_H^2(z)}{w_S^2(z)} \right\}, \quad (1)$$

where,

$$w_H^2(z) = w_0^2 \left[\left(\frac{z - z_f}{2nz_R} \right)^2 + 1 \right], \quad w_S^2(z) = w_H^2(z) + \frac{1}{3} (\mu_s z) \theta_{\text{RMS}}^2 \left(\frac{z}{n} \right)^2. \quad (2)$$

This formulation enables the network to simulate theoretical OCT intensities from the predicted optical properties (n, μ_s, g) and enforces physics-guided consistency with the measured OCT signals during training.

2.3 Loss Function

The total loss consists of four terms:

2.3.1 Parameter reconstruction loss

The mean squared error (MSE) between the predicted optical properties (n, μ_s, g) and the Monte Carlo ground truth (n^*, μ_s^*, g^*) :

$$\mathcal{L}_{\text{MSE}} = \frac{1}{|\Omega|} \sum_{(x,y) \in \Omega} \left(\|n(x,y) - n^*(x,y)\|_2^2 + \|\mu_s(x,y) - \mu_s^*(x,y)\|_2^2 + \|g(x,y) - g^*(x,y)\|_2^2 \right), \quad (3)$$

where Ω denotes the spatial domain of the OCT Bscan image.

2.3.2 Forward consistency loss

Constraints forward-model output to match the measured OCT signal:

$$\mathcal{L}_{\text{fwd}} = \frac{1}{|\Omega|} \sum_{(x,y) \in \Omega} \left\| \hat{I}_{\text{OCT}}(x,y) - I_{\text{raw}}(x,y) \right\|_2^2, \quad (4)$$

where $\hat{I}_{\text{OCT}} = \mathcal{F}_{\text{EHF}}(n, \mu_s, g)$ denotes the OCT intensity generated by the physics-based forward model.

2.3.3 Spatial regularization

Total variation (TV) regularization is applied to suppress speckle noise in the raw OCT intensity I_{raw} and to encourage spatial smoothness and continuity in the predicted parameter maps:

$$\mathcal{L}_{\text{TV}} = \sum_{p \in \{n, \mu_s, g\}} \sum_{(x, y) \in \Omega} (|\nabla_x p(x, y)| + |\nabla_y p(x, y)|), \quad (5)$$

where ∇_x and ∇_y denote spatial finite differences along the horizontal and vertical directions, respectively.

2.3.4 Diffusion-based score regularization

To further stabilize the inverse reconstruction, diffusion-model-based score regularization is incorporated as a learned statistical prior. The predicted parameter maps are first normalized and downsampled to 256×256 , then perturbed by Gaussian noise following a predefined diffusion noise schedule. The resulting noisy samples are compared with score targets produced by pretrained EDM denoisers:^{19, 20}

$$\mathcal{L}_{\text{DIFF}} = \sum_{p \in \{n, \mu_s, g\}} \omega_p \mathbb{E}_{\mathbf{x}_t} \left[\left\| s_{\theta_p}(\mathbf{x}_t, t) - s^*(\mathbf{x}_t, t) \right\|_2^2 \right], \quad (6)$$

where s_{θ_p} denotes the score function predicted by the pretrained EDM denoiser for parameter p , and s^* is the analytical score target derived from the diffusion process. And $\omega_n = 1$, $\omega_{\mu_s} = 1$, $\omega_g = 0.3$ are weighting coefficients that balance the contributions of each branch to stabilize gradient magnitudes during training. Because the EDM priors were trained on over 20,000 Monte Carlo scattering simulations, this regularization introduces a reliable statistical prior, improving robustness and convergence stability in the inverse mapping.

2.3.5 Total loss

The overall training objective is given as:

$$\mathcal{L}_{\text{total}} = \lambda_1 \mathcal{L}_{\text{MSE}} + \lambda_2 \mathcal{L}_{\text{fwd}} + \lambda_3 \mathcal{L}_{\text{TV}} + \lambda_4 \mathcal{L}_{\text{DIFF}}, \quad (7)$$

where λ_1 , λ_2 , λ_3 , and λ_4 are balancing weights.

2.4 Training and Inference

Training is performed using patch-based mini-batches on an NVIDIA A100 GPU, with learning rate 2×10^{-5} and Adam optimizer. Training is stopped when validation accuracy degrades. During inference, only a single forward pass is required to simultaneously produce speckle-reduced structural intensity and all three optical parameter maps.

3. RESULTS

3.1 Qualitative Comparisons

From the qualitative comparisons, removing diffusion regularization leads to incorrect μ_s outputs, as shown in figure 2. The recovered scattering profile no longer follows the five-layer distribution defined in the Monte Carlo modeling of light transport in multi-layered tissues (MCML) corneal model,²¹ and an additional artificial layer appears. The baseline U-Net underfits and reconstructs fewer than five layers, suggesting insufficient preservation of layer structure in the absence of appropriate priors.

All ablated variants—including the U-Net baseline and the full model without TV, diffusion, or physics-based constraints—exhibit speckle-like artifacts in the predicted OCT intensity I_s , particularly in the air and vitreous humor regions. In contrast, the proposed framework produces the cleanest and most clearly stratified layer boundaries.

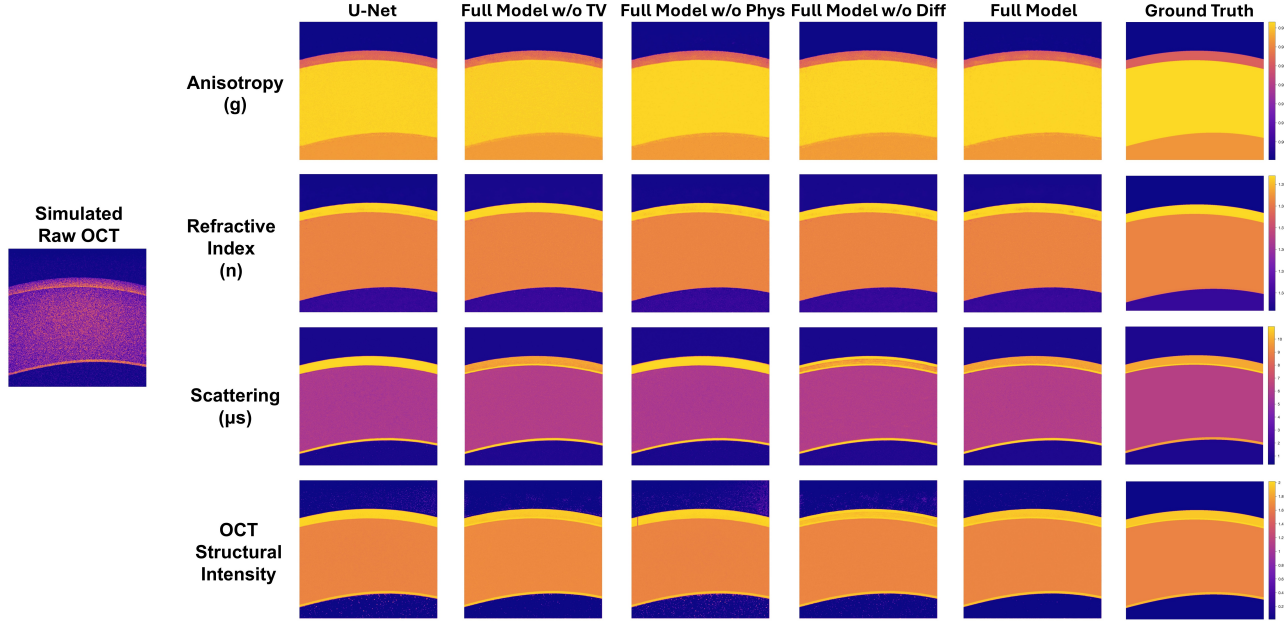


Figure 2. End-to-end reconstruction of OCT structural intensity and quantitative optical maps with ablation studies.

Table 1. Quantitative comparison on OCT structural intensity and scattering coefficient μ_s . **Bold**: best.

Model	OCT Structural Intensity			μ_s		
	PSNR \uparrow	SSIM \uparrow	MSE \downarrow	PSNR \uparrow	SSIM \uparrow	MSE \downarrow
Full Model	31.65	0.94	2.75×10^{-3}	28.03	0.70	0.23
Full Model w/o Diffusion	27.41	0.88	7.29×10^{-3}	26.46	0.73	0.33
Full Model w/o Physics	23.41	0.80	1.83×10^{-2}	24.09	0.70	0.56
Full Model w/o TV	28.74	0.92	5.3×10^{-2}	27.93	0.71	0.23
Baseline U-Net	25.04	0.85	1.2×10^{-2}	24.09	0.63	0.56

3.2 Quantitative Comparisons

Table 1 and 2 show superior quantitative performance of the proposed model across all metrics related to speckle-reduced OCT structural intensity \hat{I}_{OCT} and anisotropy g . These results indicate that multi-branch U-Nets combined with forward-model constraints improve reconstruction stability, noise suppression, and structural fidelity. Both PSNR and SSIM decrease significantly when diffusion regularization is removed, indicating that the absence of a statistical prior reduces robustness to noise. Removing the physics-based forward constraint further reduces reconstruction accuracy, with the structural intensity error increasing from 2.75×10^{-3} to 1.83×10^{-2} . Therefore, pixel-level supervision alone is insufficient to constrain parameter coupling and hinder convergence towards physically plausible solutions.

The ablation results also reveal substantially higher errors in μ_s and g when constraints are removed, whereas predictions of the refractive index n change only slightly. This behavior may be attributed to the small dynamic range of corneal refractive index (approximately 1.32–1.40¹⁸), which allows reasonable estimations even in the absence of explicit priors.

Finally, the baseline U-Net yields the lowest PSNR and SSIM and the highest MSE, revealing the limitations of purely data-driven learning. Specifically, the baseline model cannot jointly account for attenuation effects, parameter coupling, and noise amplification, and is therefore insufficient for reliable recovery of tissue optical properties from raw OCT intensity alone.

Table 2. Quantitative comparison on refractive index n and anisotropy g . **Bold**: best.

Model	n			g		
	PSNR \uparrow	SSIM \uparrow	MSE \downarrow	PSNR \uparrow	SSIM \uparrow	MSE \downarrow
Full Model	28.76	0.66	6.54×10^{-6}	29.25	0.84	1.90×10^{-6}
Full Model w/o Diffusion	28.79	0.66	6.49×10^{-6}	26.82	0.80	3.33×10^{-6}
Full Model w/o Physics	28.90	0.65	6.32×10^{-6}	28.57	0.81	2.23×10^{-6}
Full Model w/o TV	28.78	0.66	6.50×10^{-6}	24.31	0.75	5.93×10^{-6}
Baseline U-Net	29.29	0.67	5.78×10^{-6}	27.89	0.78	2.60×10^{-6}

4. CONCLUSION

In summary, we present a physics-regularized end-to-end framework for OCT inverse reconstruction that simultaneously recovers the tissue optical properties and structural information from speckle-reduced OCT intensity in a single forward pass. By embedding the physics-based forward model and diffusion-based priors, the proposed approach effectively addresses attenuation, speckle noise, and parameter coupling that commonly compromise reconstruction accuracy. Experimental results demonstrate reliable recovery of structural information directly from MCML simulated OCT Bscans of corneal tissues, highlighting the potential of physics-informed deep learning for quantitative, label-free tissue visualization.

ACKNOWLEDGMENTS

This work was supported by National Institute of Health Grant Award No. 1R01EY032127 (PI: Jin U. Kang), the study was conducted at Johns Hopkins University.

REFERENCES

- [1] Wang, Y., Wei, S., Zuo, R., Kam, M., Opfermann, J. D., Sunmola, I., Hsieh, M. H., Krieger, A., and Kang, J. U., “Automatic and real-time tissue sensing for autonomous intestinal anastomosis using hybrid mlp-dc-cnn classifier-based optical coherence tomography,” *Biomedical Optics Express* **15**(4), 2543–2560 (2024).
- [2] Wang, Y., Singh, M. S., Li, K., Yu, J., Liu, X., and Kang, J. U., “Live porcine eye model studies of subretinal injection using handheld endoscopy oct integrated injector,” *Investigative Ophthalmology & Visual Science* **65**(7), 5499–5499 (2024).
- [3] Wang, Y., Opfermann, J., Yu, J., Yi, H., Kaluna, J., Biswas, R., Zuo, R., Gensheimer, W., Krieger, A., and Kang, J., “Reimagining partial thickness keratoplasty: An eye mountable robot for autonomous big bubble needle insertion,” *arXiv preprint arXiv:2410.14577* (2024).
- [4] Yu, J., Yi, H., Wang, Y., Opfermann, J. D., Gensheimer, W. G., Krieger, A., and Kang, J. U., “Topology-based deep-learning segmentation method for deep anterior lamellar keratoplasty (dalk) surgical guidance using m-mode oct data,” in [*Optical Fibers and Sensors for Medical Diagnostics, Treatment, and Environmental Applications XXV*], **13310**, 7–13, SPIE (2025).
- [5] Yi, H., Yu, J., Wang, Y., Opfermann, J., Gensheimer, B. G., Krieger, A., and Kang, J. U., “Kalman filter/deep-learning hybrid automatic boundary tracking of optical coherence tomography data for deep anterior lamellar keratoplasty (dalk),” in [*Optical Fibers and Sensors for Medical Diagnostics, Treatment, and Environmental Applications XXV*], **13310**, 59–65, SPIE (2025).
- [6] Xu, J., Yu, J., Yao, J., and Zhang, R., “The neural networks-based needle detection for medical retinal surgery,” in [*International Conference on Computer Graphics, Artificial Intelligence, and Data Processing (ICCAID 2022)*], **12604**, 674–678, SPIE (2023).
- [7] Wang, Y., Wei, S., and Kang, J. U., “Depth-resolved backscattering signal reconstruction based oct attenuation compensation,” in [*Proceedings of SPIE—the International Society for Optical Engineering*], **11953**, 119530D (2022).
- [8] Wang, Y., Wei, S., Guo, S., and Kang, J. U., “Optimized oct-based depth-resolved model for attenuation compensation using point-spread-function calibration,” in [*Optical Fibers and Sensors for Medical Diagnostics, Treatment and Environmental Applications XXI*], **11635**, 35–40, SPIE (2021).

- [9] Wang, Y., *OPTICAL COHERENCE TOMOGRAPHY BASED OPHTHALMIC AND GASTROINTESTINAL SURGICAL GUIDANCE USING DEEP LEARNING*, PhD thesis, Johns Hopkins University (2024).
- [10] Wang, Y., Wei, S., and Kang, J. U., “Depth-dependent attenuation and backscattering characterization of optical coherence tomography by stationary iterative method,” *Journal of Biomedical Optics* **28**(8), 085002–085002 (2023).
- [11] Chang, S., Flueraru, C., Mao, Y., and Sherif, S., “Attenuation compensation for optical coherence tomography imaging,” *Optics Communications* **282**(23), 4503–4507 (2009).
- [12] Vermeer, K. A., Mo, J., Weda, J. J., Lemij, H. G., and de Boer, J. F., “Depth-resolved model-based reconstruction of attenuation coefficients in optical coherence tomography,” *Biomedical Optics Express* **5**(1), 322–337 (2013).
- [13] Cannon, T. M., Bouma, B. E., and Uribe-Patarroyo, N., “Layer-based, depth-resolved computation of attenuation coefficients and backscattering fractions in tissue using optical coherence tomography,” *Biomedical Optics Express* **12**(8), 5037–5056 (2021).
- [14] Li, K., Liang, W., Yang, Z., Liang, Y., and Wan, S., “Robust, accurate depth-resolved attenuation characterization in optical coherence tomography,” *Biomedical Optics Express* **11**(2), 672–687 (2020).
- [15] Wang, Y., Yu, J., Guo, W., Sun, Y., and Kang, J. U., “Super-resolution optical coherence tomography using diffusion model-based plug-and-play priors,” *arXiv preprint arXiv:2505.14916* (2025).
- [16] Zuo, R., Wei, S., Wang, Y., Irsch, K., and Kang, J. U., “High-resolution *in vivo* 4d-oct fish-eye imaging using 3d-unet with multi-level residue decoder,” *Biomedical Optics Express* **15**(9), 5533–5546 (2024).
- [17] Gerakis, A., Kirillin, M. Y., Sergeeva, E. A., Makropoulou, M., and Serafetinides, A., “Monte carlo modeling of corneal and retinal optical coherence tomography imaging,” in [2008 8th IEEE International Conference on BioInformatics and BioEngineering], 1–6, IEEE (2008).
- [18] Gong, P., Almasian, M., Van Soest, G., De Bruin, D. M., Van Leeuwen, T. G., Sampson, D. D., and Faber, D. J., “Parametric imaging of attenuation by optical coherence tomography: review of models, methods, and clinical translation,” *Journal of Biomedical Optics* **25**(4), 040901–040901 (2020).
- [19] Karras, T., Aittala, M., Aila, T., and Laine, S., “Elucidating the design space of diffusion-based generative models,” *Advances in Neural Information Processing Systems* **35**, 26565–26577 (2022).
- [20] Guo, W., Yu, J., Wang, Y., Kang, J. U., and Sun, Y., “Psi3d: Plug-and-play 3d stochastic inference with slice-wise latent diffusion prior,” *arXiv preprint arXiv:2512.18367* (2025).
- [21] Wang, L., Jacques, S. L., and Zheng, L., “MCML—Monte Carlo modeling of light transport in multi-layered tissues,” *Computer Methods and Programs in Biomedicine* **47**(2), 131–146 (1995).